Supplementary Information (SI) for Journal of Materials Chemistry A.
This journal is © The Royal Society of Chemistry 2026

Tailoring Plasmonic Sensitivity through Functional MXene–MOF Hybrids for High-Performance PIERS Detection of Pharmaceutical Molecules

Himanshu Yadav,[1#] Mugdha Chaturvedi,[2#] Ruchi Singh,[1] Balla Putrakumar,[3] Saandra Sharma,[2] Rabindranath Lo,[4] Soumik Siddhanta[1]* and Kolleboyina Jayarmaulu[2]*

[1]Department of Chemistry, Indian Institute of Technology Delhi, Hauz Khas, New Delhi – 110016, India

[2]Hybrid Porous Materials Laboratory, Department of Chemistry, Indian Institute of Technology Jammu, Jammu & Kashmir, 181221, India

[3]Department of Chemical Engineering and Applied Chemistry, Chungnam National University Daejeon, 34134, Republic of Korea

[4]Institute of Organic Chemistry and Biochemistry, Czech Academy of Sciences, v.v.i., Flemingovo nám. 2, 160 00 Prague 6, Czech Republic

Email (s): soumik@iitd.ac.in; jayaramulu.kolleboyina@iitjammu.ac.in

#H.Y and M.C equally contributed to this work

Keywords: Metal-Organic Frameworks (MOFs), MXene, Plasmon-Enhanced Raman Spectroscopy (PIERS), density functional theory (DFT), Pharmaceutical Molecules.

1. Experimental Section

1.1 Characterization Techniques

XRD measurements were performed using X'Pert PRO MPD diffractometer (PANalytical) in the Bragg–Brentano geometry equipped with a Co X-ray tube. Samples were placed on a zero-background Si slide, gently pressed, and scanned with a step size of 0.0334°, and the 2θ range of 5°–120° was used to record the pattern. The Le-Bail profile fitting was performed on all materials using the FullProf suite and the lattice parameters determined are listed in Table S1. Infra-red spectra were acquired using an iS5 FTIR spectrometer (Thermo Nicolet) with the Smart Orbit ATR accessory featuring a ZnSe crystal. A drop of sample dispersion in ethanol or water was placed on a ZnSe crystal, left to dry forming a film in ambient conditions, and spectra were recorded by summing 50 scans. X-ray photoelectron spectroscopy (XPS) was conducted using a PHI VersaProbe II (Physical Electronics) spectrometer with an Al Kα source (15 kV, 50 W, spot size 100 μm). Binding energies were referenced to the C1s core level of the C-C bond at the nominal value of 284.8 eV. Transmission electron microscopy (TEM) images were obtained using a JEOL 2100 TEM with an emission gun of LaB6 type operating at 160 kV. High-resolution TEM images were obtained using an FEI Titan electron microscope operating at 80 kV. Scanning electron microscopy (SEM) was performed using a Hitachi SU6600 instrument with an accelerating voltage of 5 kV. N_2 adsorption measurements were performed at 77 K using a Quantachrome automated volumetric system with a liquid nitrogen bath. Prior to analysis, samples were degassed under vacuum at 120 °C for 12 hours.The morphological characterization of the samples was performed using field emission scanning electron microscopy (SEM, SU810, Hitachi, Japan), equipped with an energy-dispersive X-ray spectroscope (EDS), operating at an accelerating voltage of 10 kV. To avoid sample charging, a thin layer of gold was sputter-coated onto the samples prior to analysis using an SCD Union sputter coater.

2. Analytical Performance Evaluation

2.1 Limit of Detection (LOD) Calculation

The limit of detection (LOD) of the PIERS substrate was estimated using the calibration curve obtained from concentration-dependent Raman measurements of 4-nitrothiophenol (4-NTP). The calibration curve was constructed by plotting the logarithm of Raman intensity against the logarithm of analyte concentration according to the following equation:

$$Y = A + B \times \log(C) \quad \#(1)$$

where A and B represent the intercept and slope of the linear regression obtained from the plot of logarithmic Raman intensity (Y) versus logarithmic concentration (C).

The LOD was calculated using the following equation:

$$LOD = 10^{\frac{(Y_{blank} + 3SD - A)}{B}} \quad \#(2)$$

where Y_{blank} is the Raman signal obtained from the blank sample and SD represents the standard deviation of the blank measurements.

The standard deviation was calculated using:

$$SD = \sqrt{\frac{\sum_{i=1}^{n}(x_i - x_{avg})^2}{n-1}} \#(3)$$

where $x_i$represents the Raman intensity of the blank measurement and $x_{avg}$is the average blank signal obtained from repeated measurements.

2.2 Enhancement Factor (EF) Calculation

The SERS and PIERS enhancement factors were calculated using the following equation:

$$EF = \frac{I_{SERS\ or\ PIERS}}{I_{Raman}} \times \frac{N_{bulk}}{N_{surface}} \#(4)$$

where I_{SERS} and I_{Raman} represent the Raman intensity of the analyte molecule recorded with and without the SERS substrate, respectively. N_{bulk} corresponds to the number of molecules probed in the conventional Raman measurement, while $N_{surface}$ represents the number of molecules contributing to the SERS and PIERS signal on the substrate.

The number of molecules in the bulk Raman measurement is given by:

$$N_{bulk} = \frac{A_{laser} \times h \times \rho}{M} \times N_A \#(5)$$

where A_{laser} is the laser spot area, h is the penetration depth [$\left(h = \frac{n\lambda}{(NA)^2}\right)$; n is the refractive index, λ is the excitation wavelength and NA is the numerical aperture of probe], ρ is the density of the analyte, M is its molecular weight, and N_A is Avogadro's number.

Together, the product of A_{laser} and h is defined as the volume of a focused laser spot.

Since 4-NTP contains a thiol group, it can chemisorb on the Au-containing substrate through Au-S bonding. Therefore, for estimating N_{surface}, we assumed monolayer-type surface coverage of 4-NTP on the Au surface. The surface density was estimated from the reported molecular footprint of 4-NTP on Au. Using an area of $39\ A^{\circ 2} molecules^{-1}$, the surface density was found to be ~ 2.56×10^{14} molecules cm^{-2}. [1, 2]

This value was used as an approximate surface coverage for calculating the number of surface-bound 4-NTP molecules contributing to the SERS/PIERS response.

The number of molecules probed in the SERS measurement can be estimated as:

$$N_{surface} = C \times A_{laser}$$

where C is the surface density of the analyte.

So, the overall expression becomes:

$$EF_{SERS\ or\ PIERS} = \frac{I_{SERS\ or\ PIERS}}{I_{Raman}} \times \frac{h \times \rho \times N_A}{M \times C} \#(7)$$

In our case, NA = 0.37, h = 7.6 µm, ρ = 1.36 g/mL, M (4-NTP) = 155.17 g/mol, C = 2.56×10^{14} molecules/cm^2, I_{Raman}= 185, I_{SERS}= 854, I_{PIERS}= 4369, EF_{SERS}= 0.73×10^5 & EF_{PIERS} = 0.37×10^6

Table S1: Table for the comparison with other substrates:

Substrate System	SERS	PIERS	Porous analyte hosting	CT pathway	Interface tailoring	References
TiO_2 + Ag/Au	✓	✓	✗	✓	✗	[3, 4]
Metal Organic Framework (MOFs)	✓	✗	✓	✗	✗	[5,6]
Covalent Organic Framework (COFs)	✓	✗	✓	✗	✓	[7, 8]
TiMXene/Au	✓	✓	✗	✓	✗	[9]
TiMXene/TiO_2/Au	✓	✓	✗	✓	✗	[10]
TiMXene/MOF/Au	✓	✓	✓	✓	✓	This work

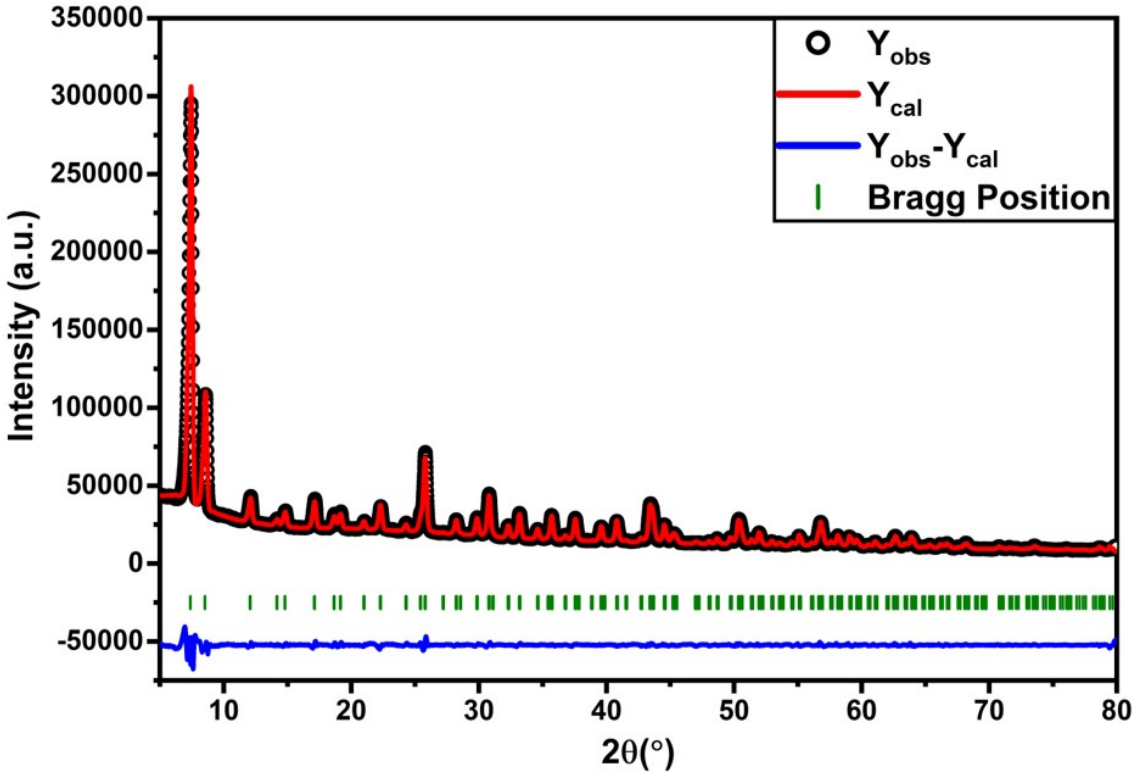

Figure S1. Le-Bail profile fitting of PXRD pattern of UiO-66-SH_2

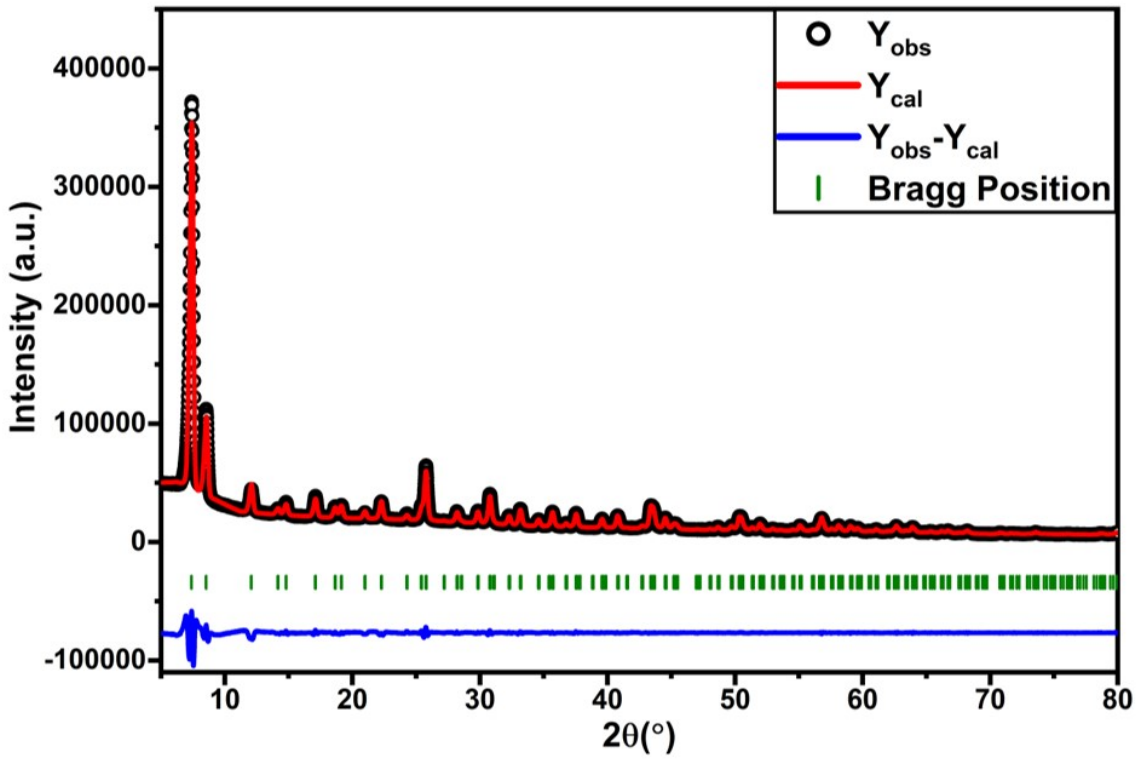

Figure S2. Le-Bail profile fitting of PXRD pattern of UiO-66-NH_2

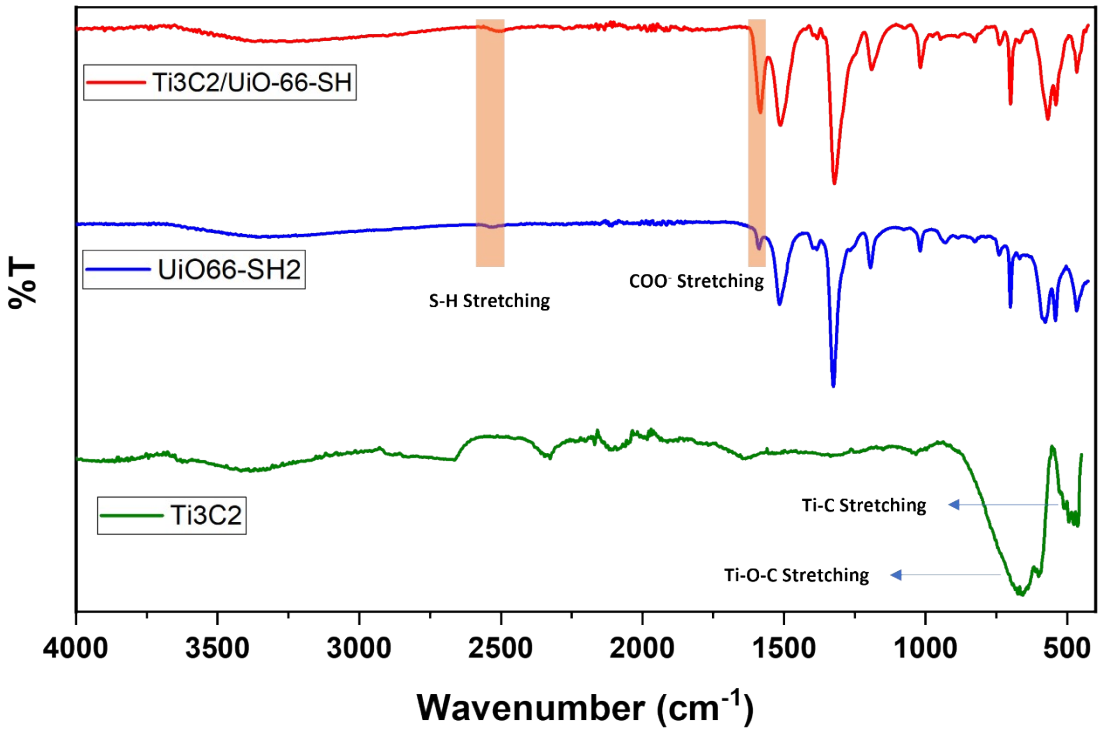

Figure S3. FTIR spectra of Ti3C2, UiO-66-SH3, and Ti3C2/UiO-66-SH hybrid. The characteristic bands at 2570 cm^{-1} and 1590 cm^{-1} correspond to S–H and COO^- stretching vibrations, respectively, confirming the presence of thiol-functionalized UiO-66. The peaks around 670 cm^{-1} and 560 cm^{-1} are attributed to Ti–C and Ti–O–C stretching modes of Ti_3C_2, respectively, indicating successful hybrid formation.

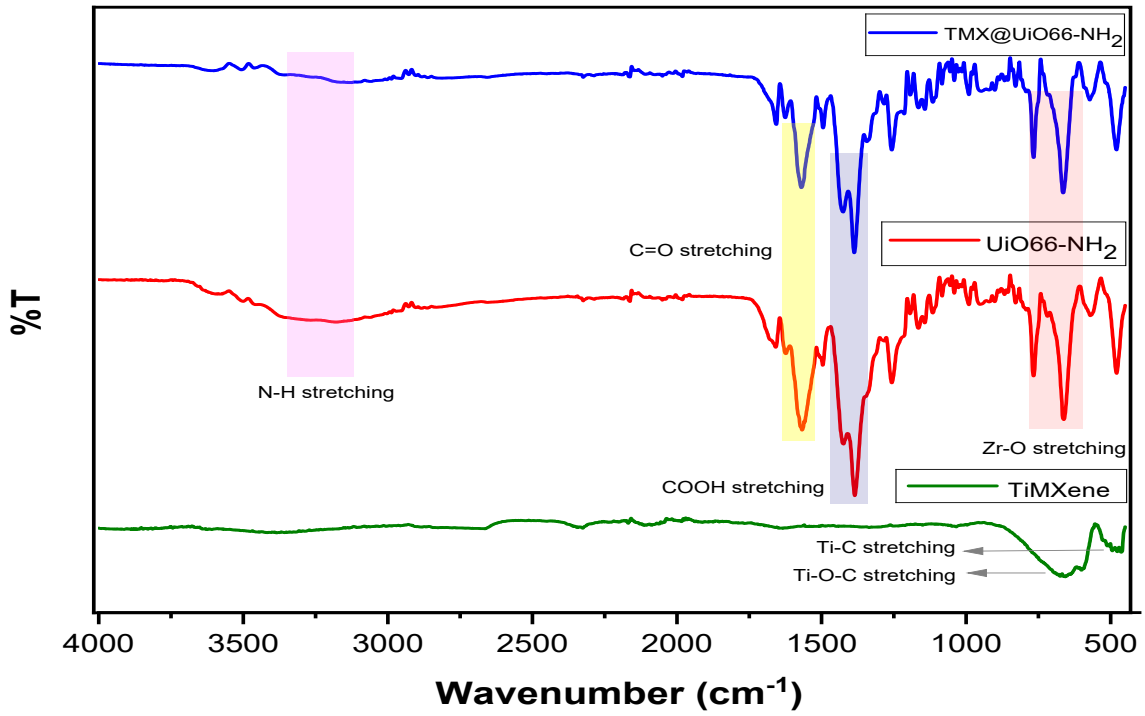

Figure S4. FTIR spectra of Ti3C2, UiO-66-SH3, and Ti3C2/UiO-66-NH_2 hybrid.

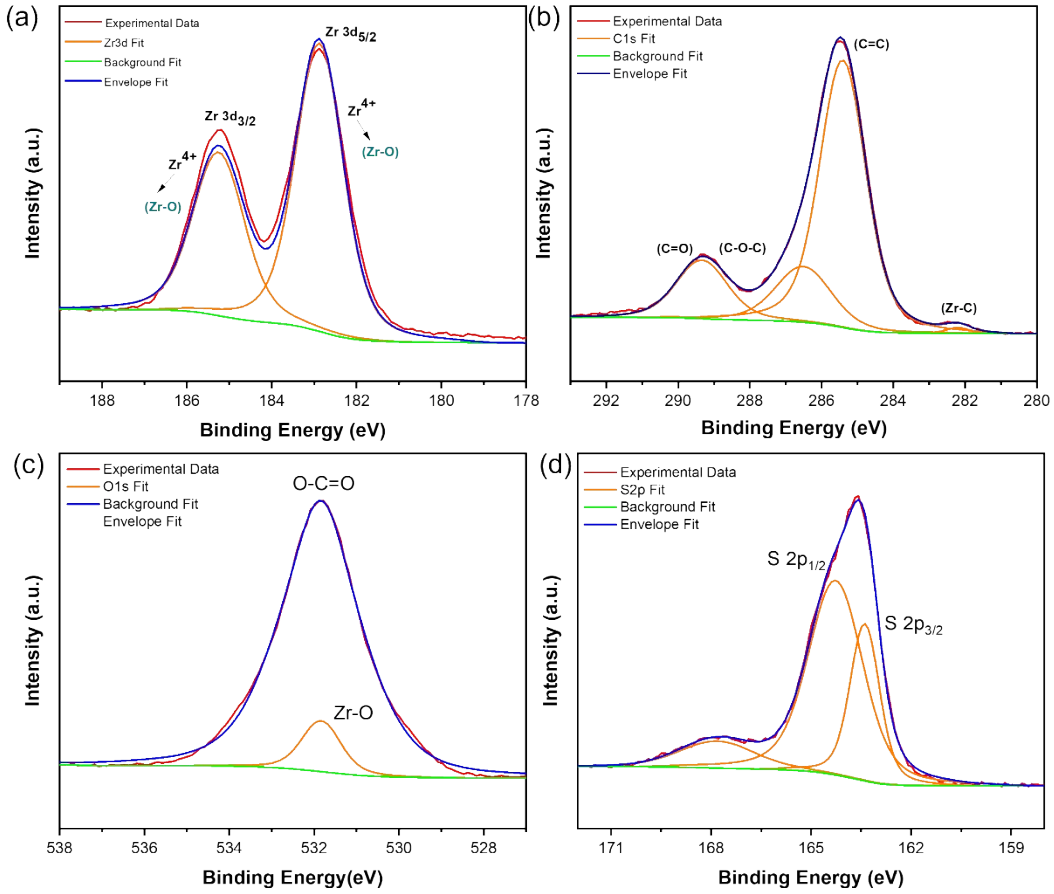

Figure S5. XPS spectra of UiO-66-SH_2 (a) Zr 3d, (b) C 1s, (c) O 1s, and (d) S 2p

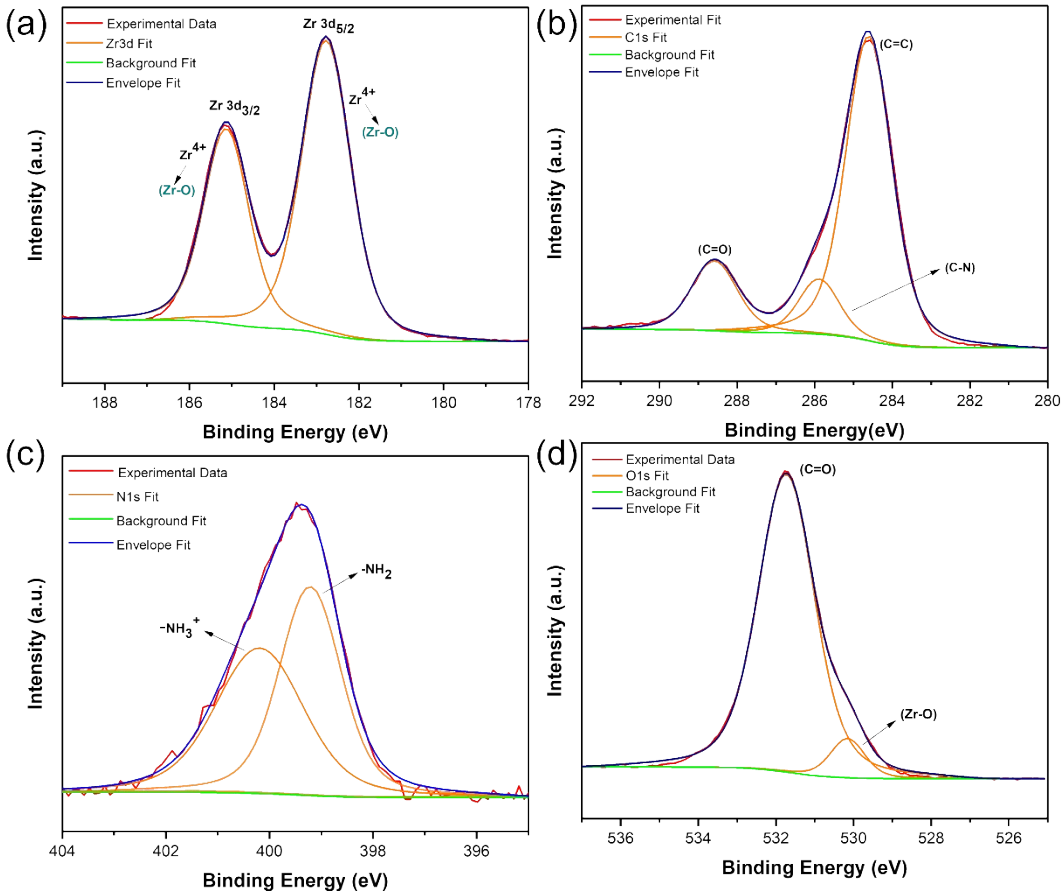

Figure S6. XPS spectra of UiO-66-NH_2 (ca) Zr 3d, (b) C 1s, (c) O 1s, and (d) N 1s.

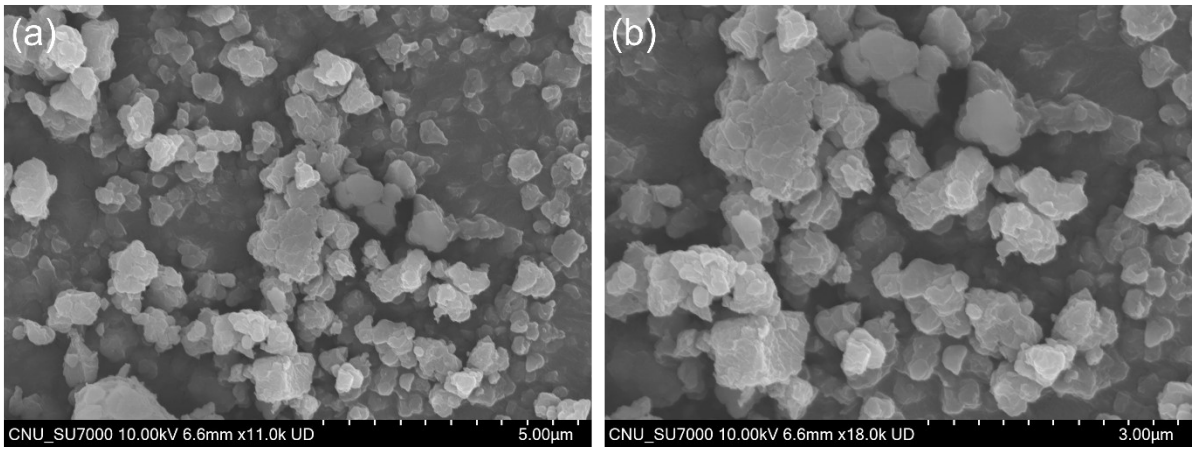

Figure S7a.. FESEM images of UiO-66-NH_2 shows irregular spherical nanoparticles

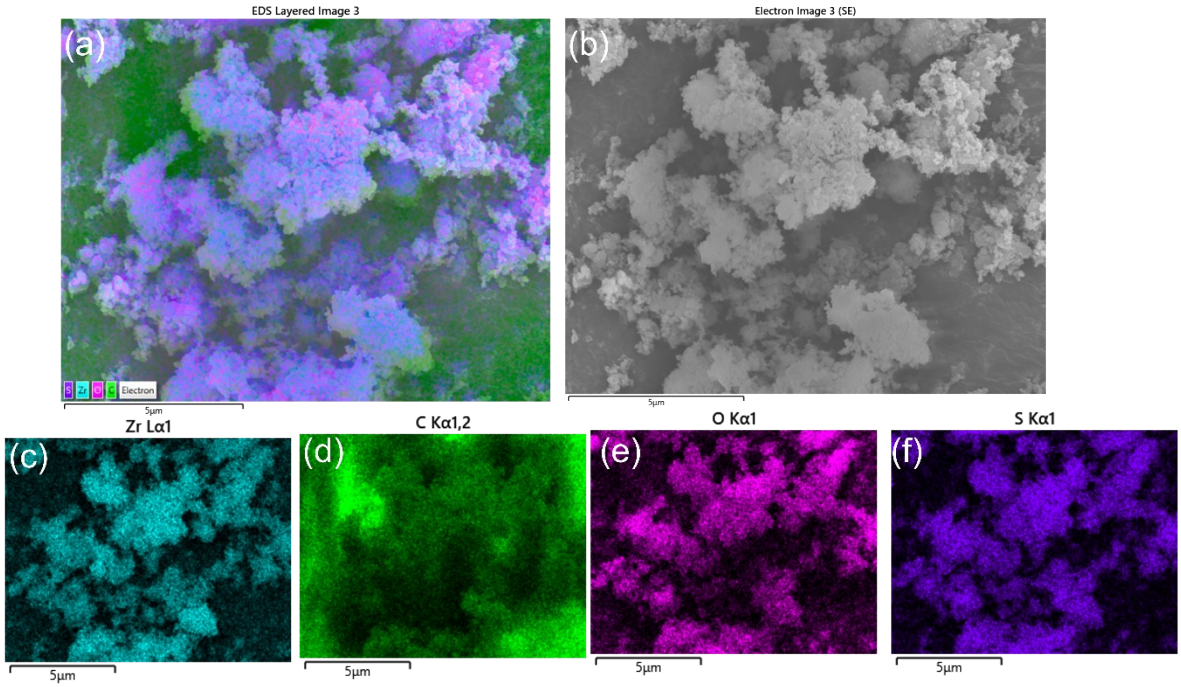

Figure S7b. EDS analysis UiO-66-SH_2 (a) irregular spherical particles (b) combined mapping of Zr, C, S and O (c) Zr; (d) C; (e) O and (f) S.

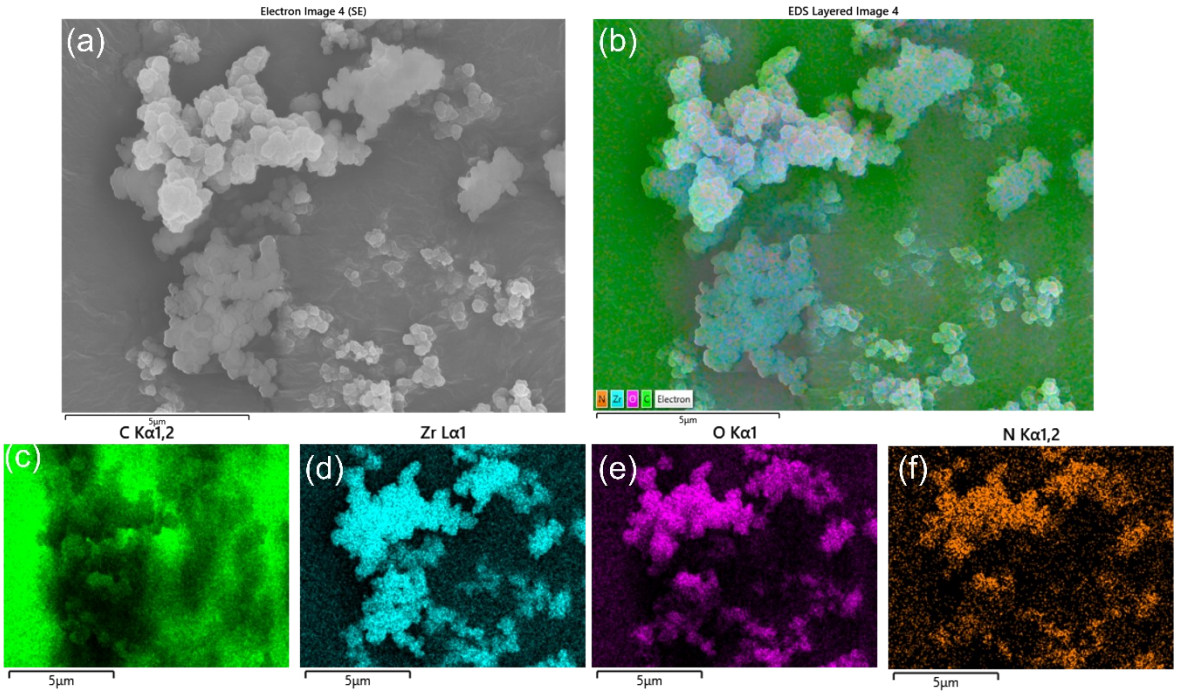

Figure S8. FESE and EDS analysis UiO-66-NH_2 (a) irregular spherical particles (b) combined mapping of Zr, C, N and O (c) C; (d) Zr; (e) O and (f) N.

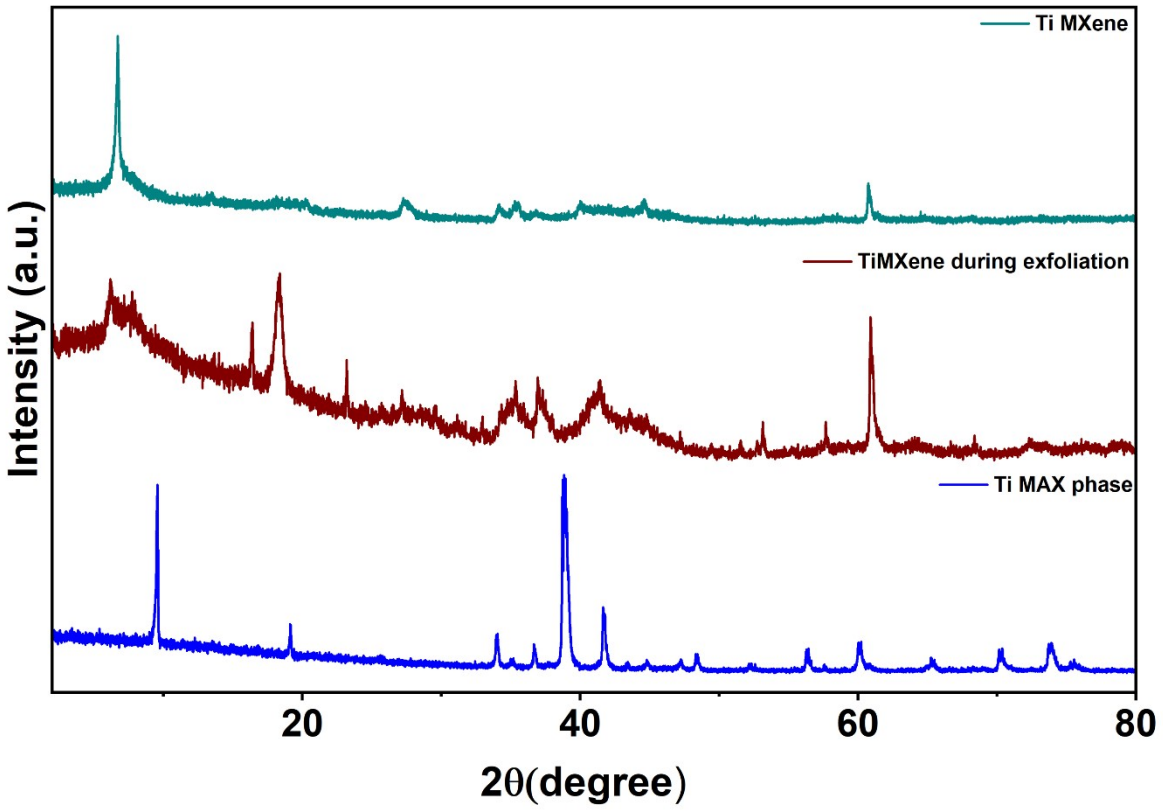

Figure S9. Powder XRD patterns of Ti-based materials showing the structural evolution from Ti MAX phase (blue) to Ti MXene during exfoliation (red) and the final Ti MXene (teal). The progressive shift and broadening of the (002) peak indicate successful exfoliation and increased interlayer spacing.

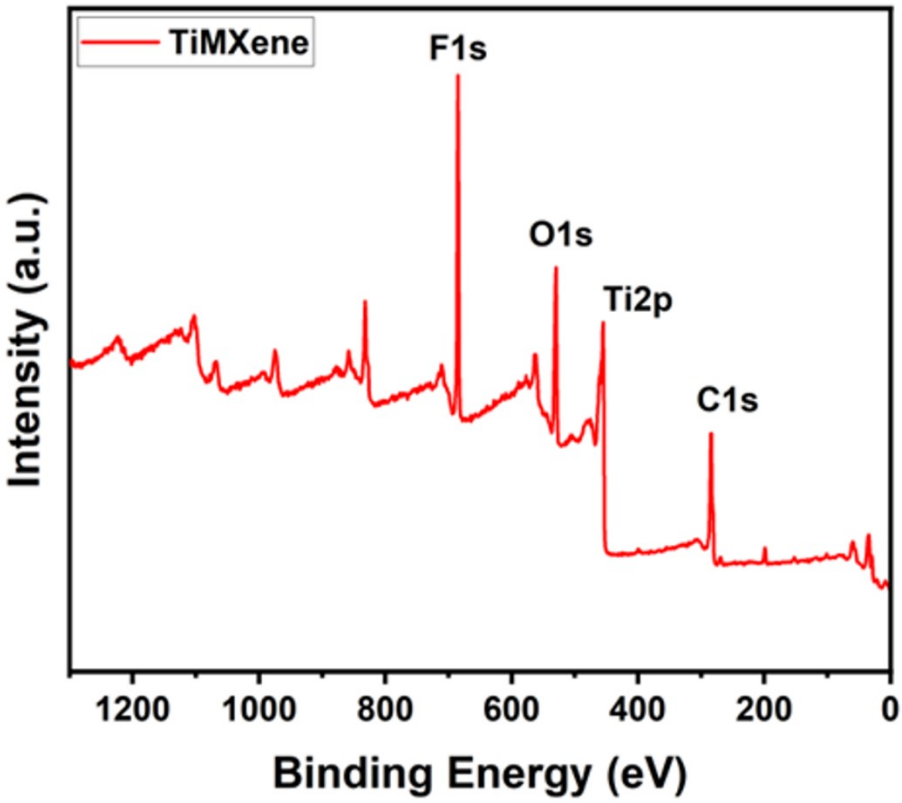

Figure S10. Survey Spectra of Ti-MXene Ti_3C_2

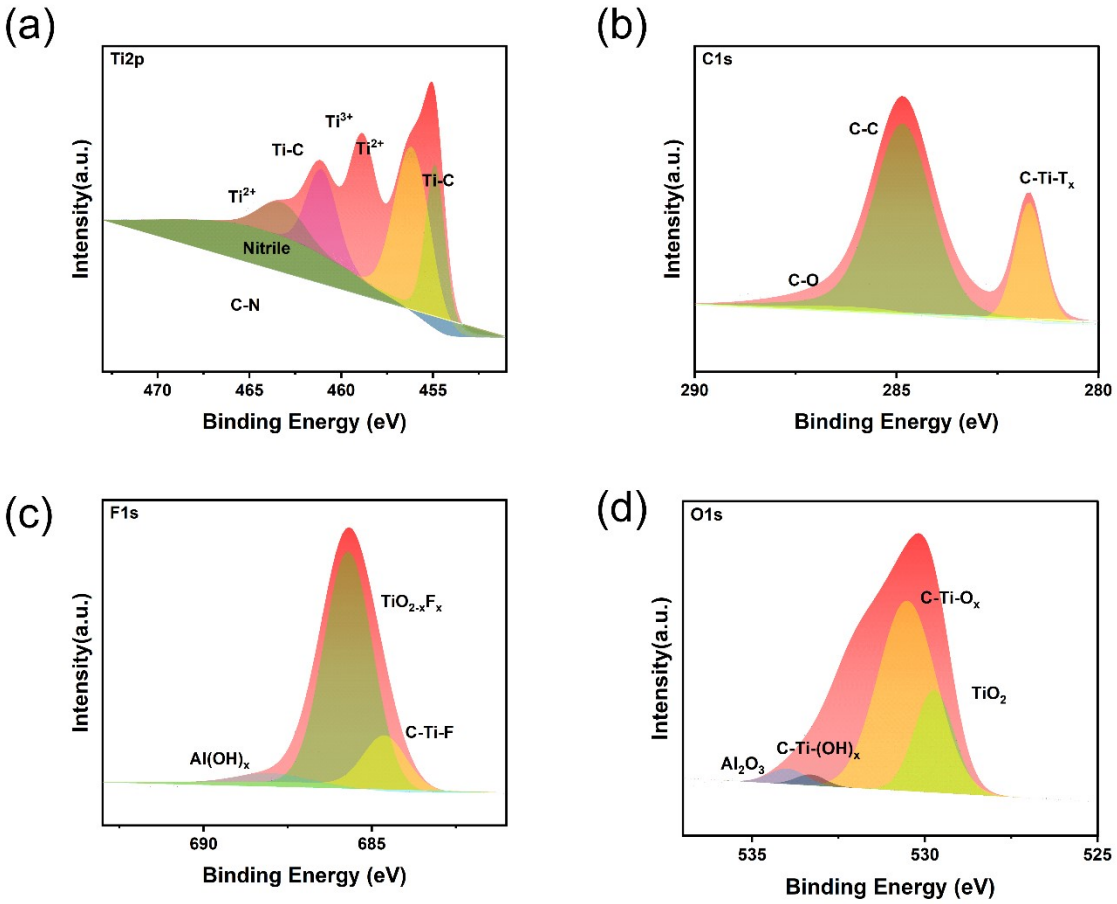

Figure S11. XPS spectra of Ti-MXene (ca) Ti3d, (b) C 1s, (c) F 1s, and (d) O 1s.

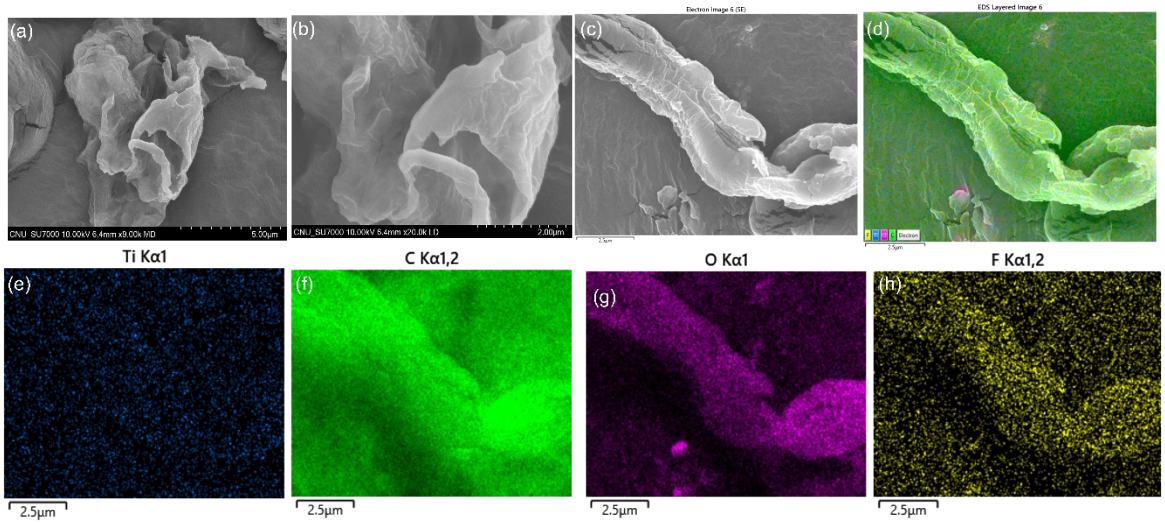

Figure S12. FESE and EDS analysis of TiMXene (a-c) layer morphology TiMXene (d) combined mapping Ti, C, O and F (e) Ti; (f) C; (g) O and (h) F.

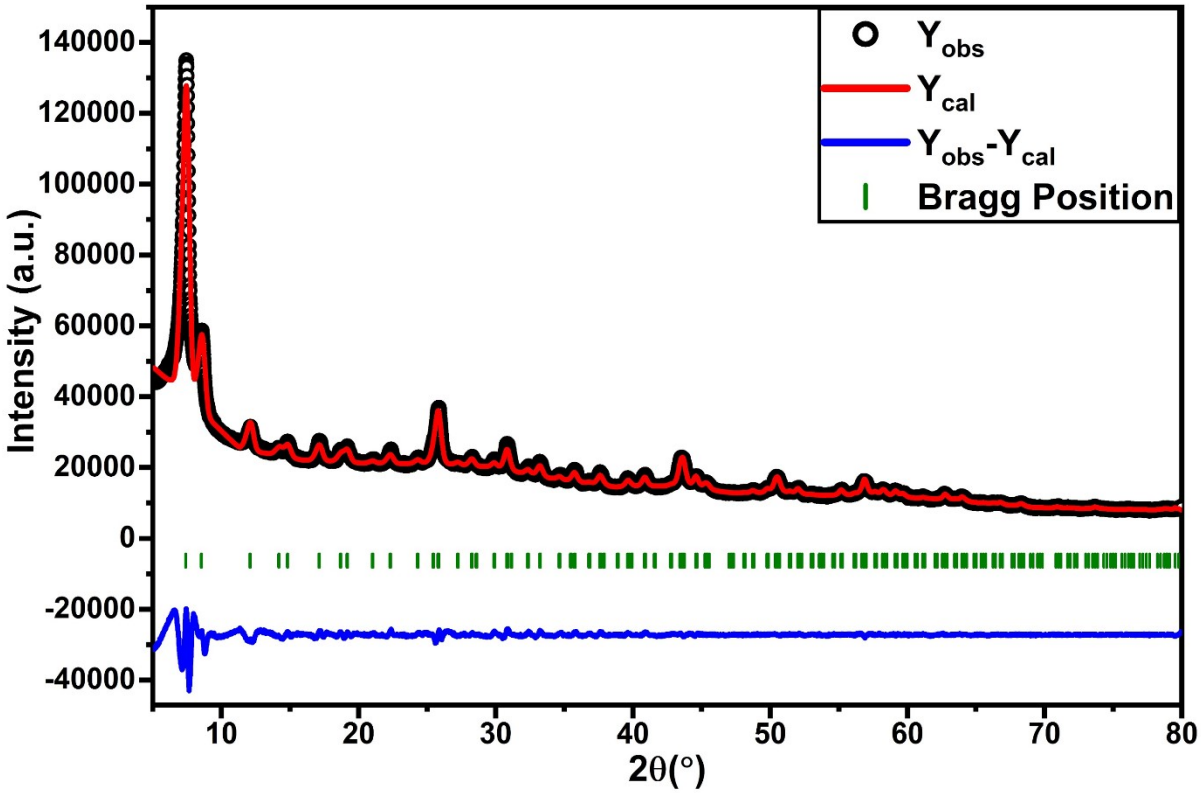

Figure S13. Le-Bail profile fitting of PXRD pattern of Ti3C2/UiO-66-SH2

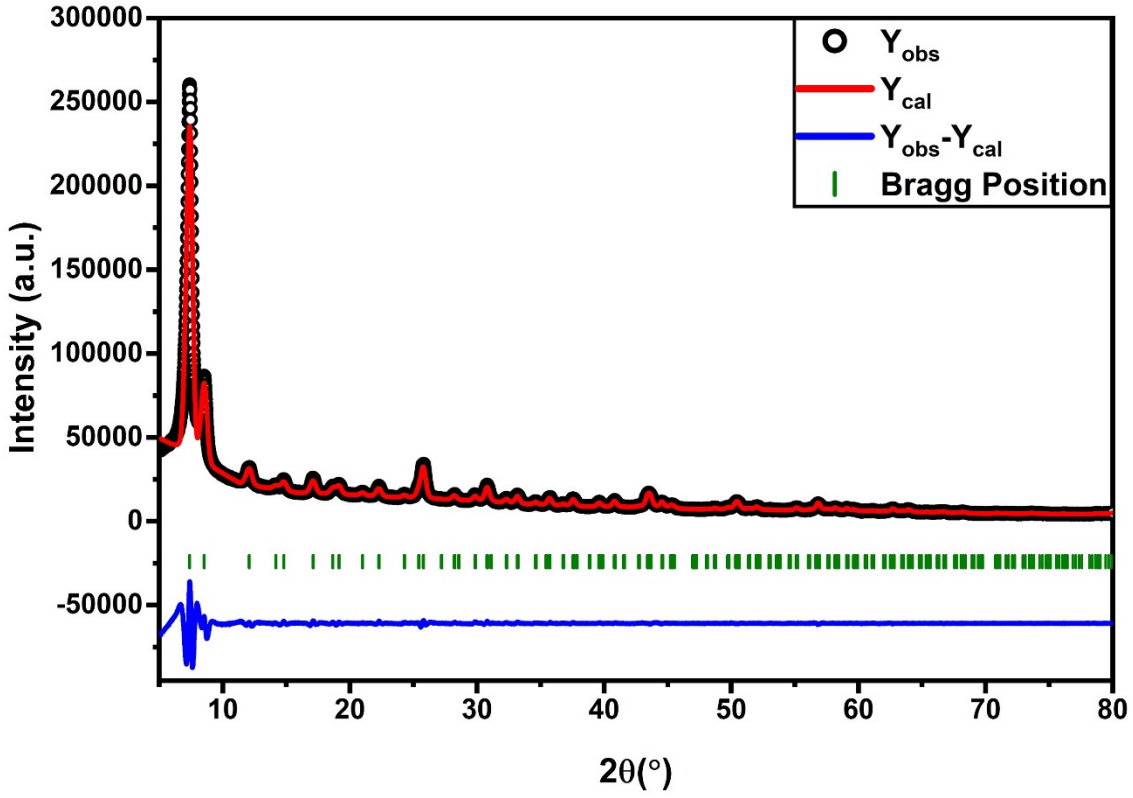

Figure S14. Le-Bail profile fitting of PXRD pattern of Ti3C2/UiO-66-NH2

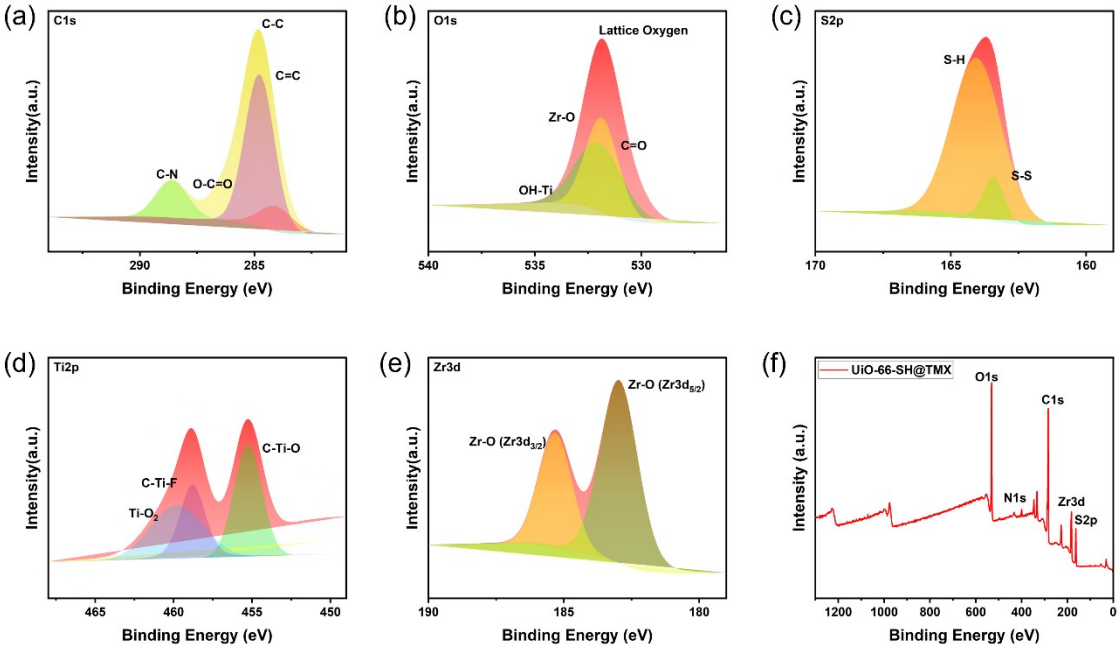

Figure S15. XPS spectra of Ti_3C_2/UiO-66-SH_2 hybrid: (a) C 1s, (b) O 1s, (c) S 2p, (d) Ti 2p, (e) Zr 3d, and (f) XPS survey spectrum.

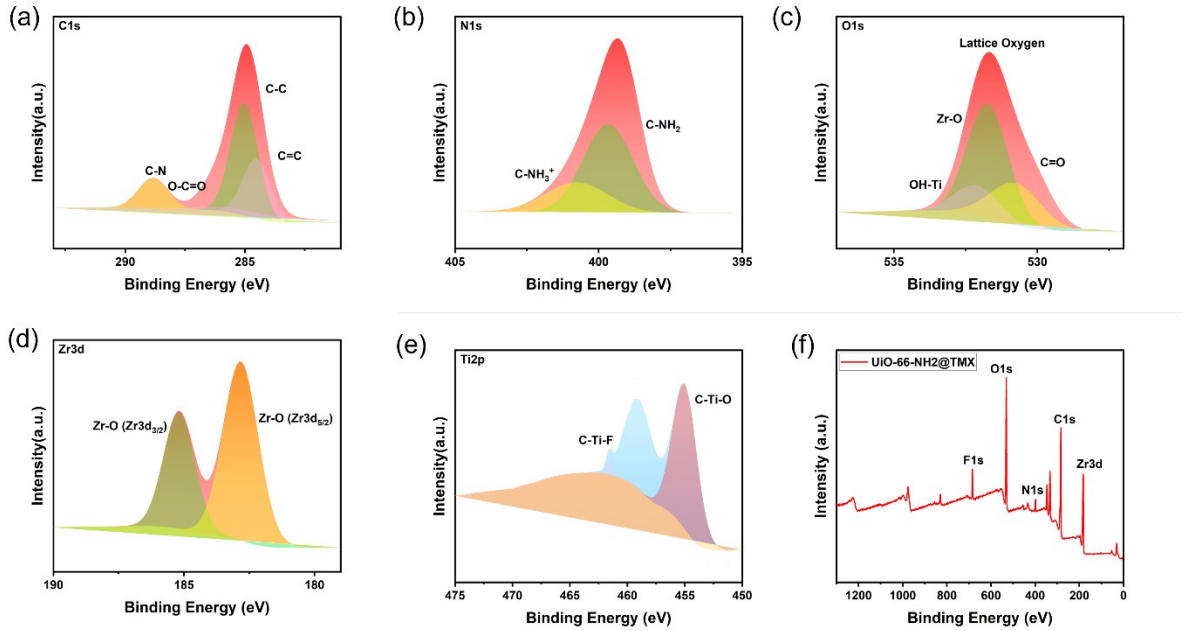

Figure S16. XPS spectra of Ti_3C_2/UiO-66-NH_2 hybrid: (a) C 1s, (b) N 1s, (c) O 1s, (d) Zr 3d (e) Ti 2p, and (f) XPS survey spectrum.

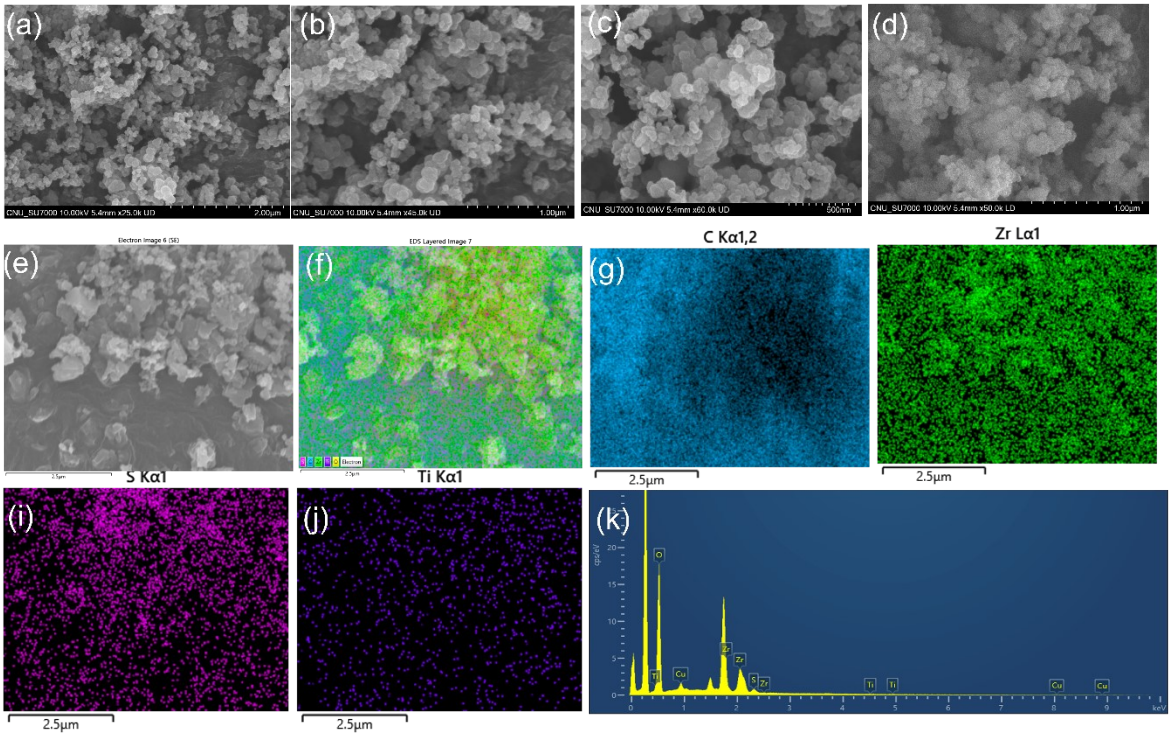

Figure S17. SEM images and corresponding EDS elemental mapping of the Ti_3C_2/UiO-66-SH_2. (a–e) SEM images showing spherical UiO-66-SH_2 nanocrystals uniformly anchored on Ti_3C_2 MXene nanosheets, forming a well-dispersed hybrid architecture. Elemental maps of (f) combined elements, (g) carbon (h) zirconium, (i) Sulphur (j) titanium (Ti) (k) EDS analysis confirm the homogeneous distribution of all elements.

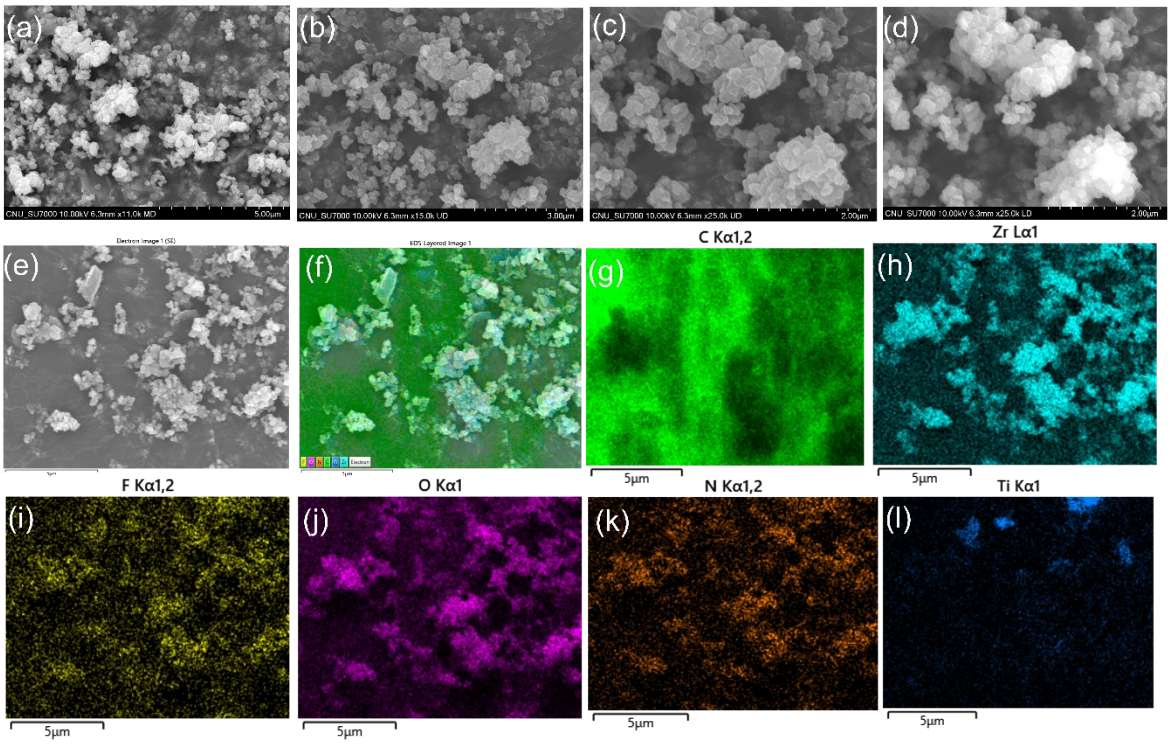

Figure S18. SEM images and corresponding EDS elemental mapping of the Ti_3C_2/UiO-66-NH_2. (a-e) The spherical UiO-66-NH_2 nanocrystals are uniformly anchored on Ti_3C_2 MXene nanosheets, forming a well-dispersed hybrid architecture. Elemental maps of (f) combined elemental mapping ; (g) Oxygen ; (h) Zirconium; (i) Fluorine; (j) Oxygen; (k) Nitrogen; (l) Titanium.

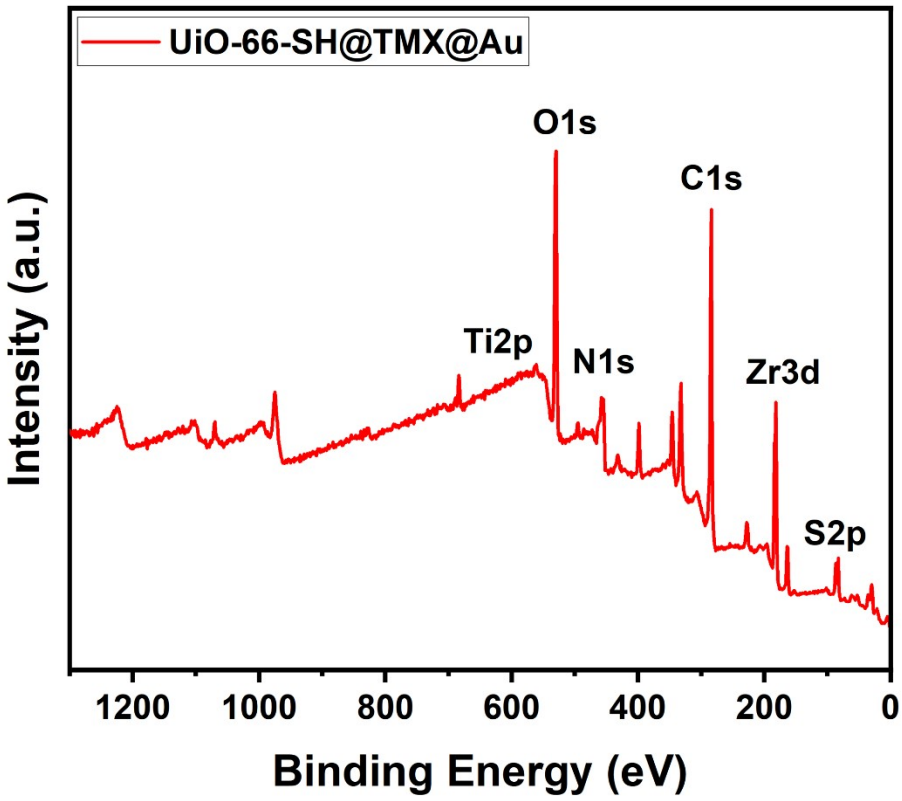

Figure S19. Survey Spectrum of Ti_3C_2/UiO-66-SH_2@Au

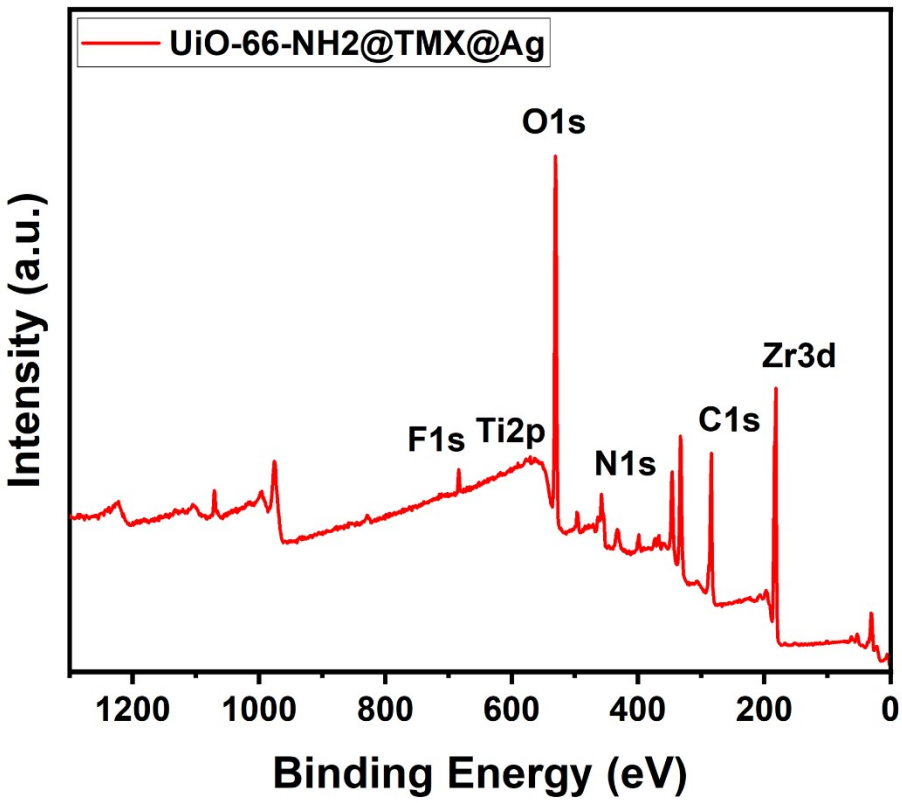

Figure S20. Survey Spectrum of Ti_3C_2/UiO-66-NH_2@Ag

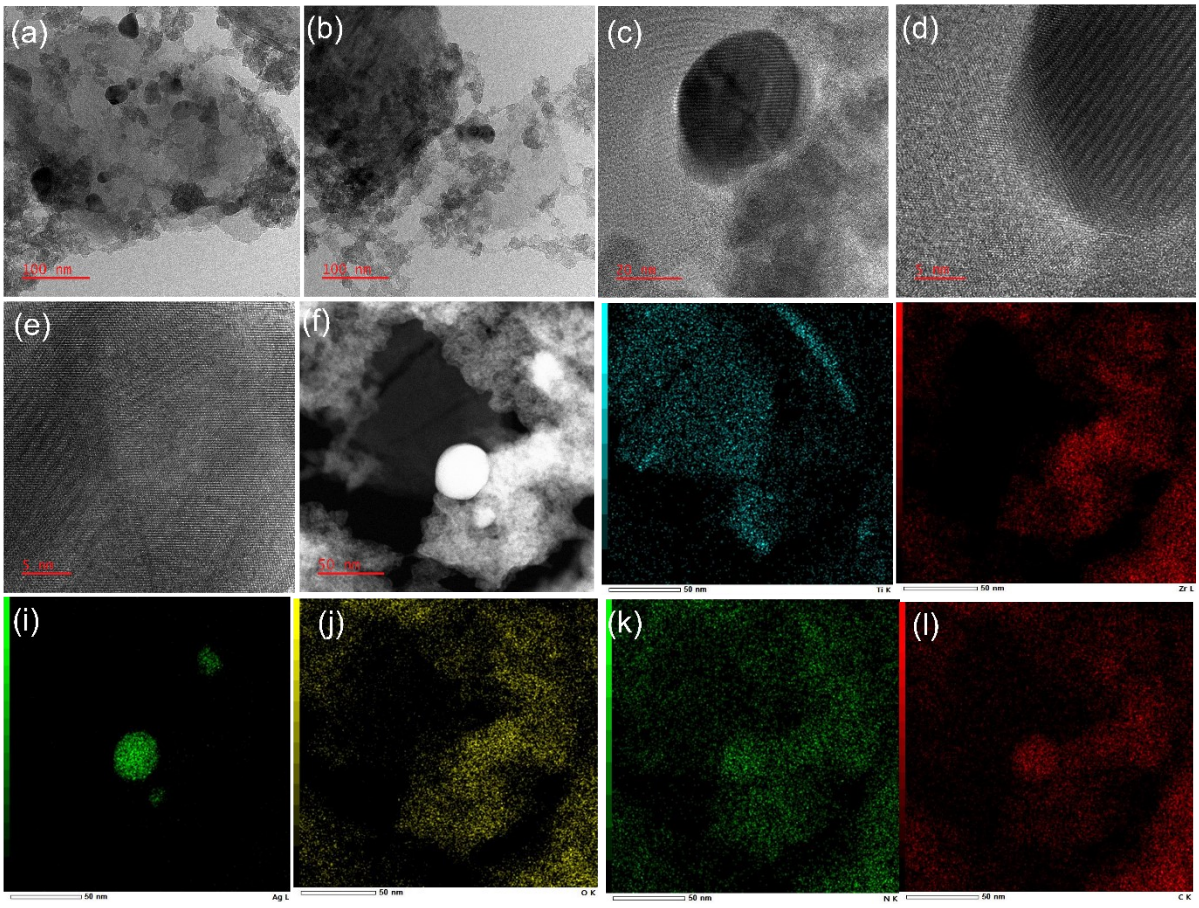

Figure S21. TEM, HRTEM, and HAADF-STEM analyses of the hybrid 2. (a–c) TEM images showing Ti_3C_2 sheets uniformly decorated with UiO-66-NH_2 nanoparticles. (d–e) HRTEM images revealing well-defined lattice fringes corresponding to Ti_3C_2, UiO-66-NH_2, and intercalated Ag nanoparticles. (f) HAADF-STEM image of the hybrid. (g–l) Elemental mapping confirming the homogeneous spatial distribution of Ti, Zr, N, Ag, C, and O, demonstrating the uniform incorporation of Ag nanoparticles

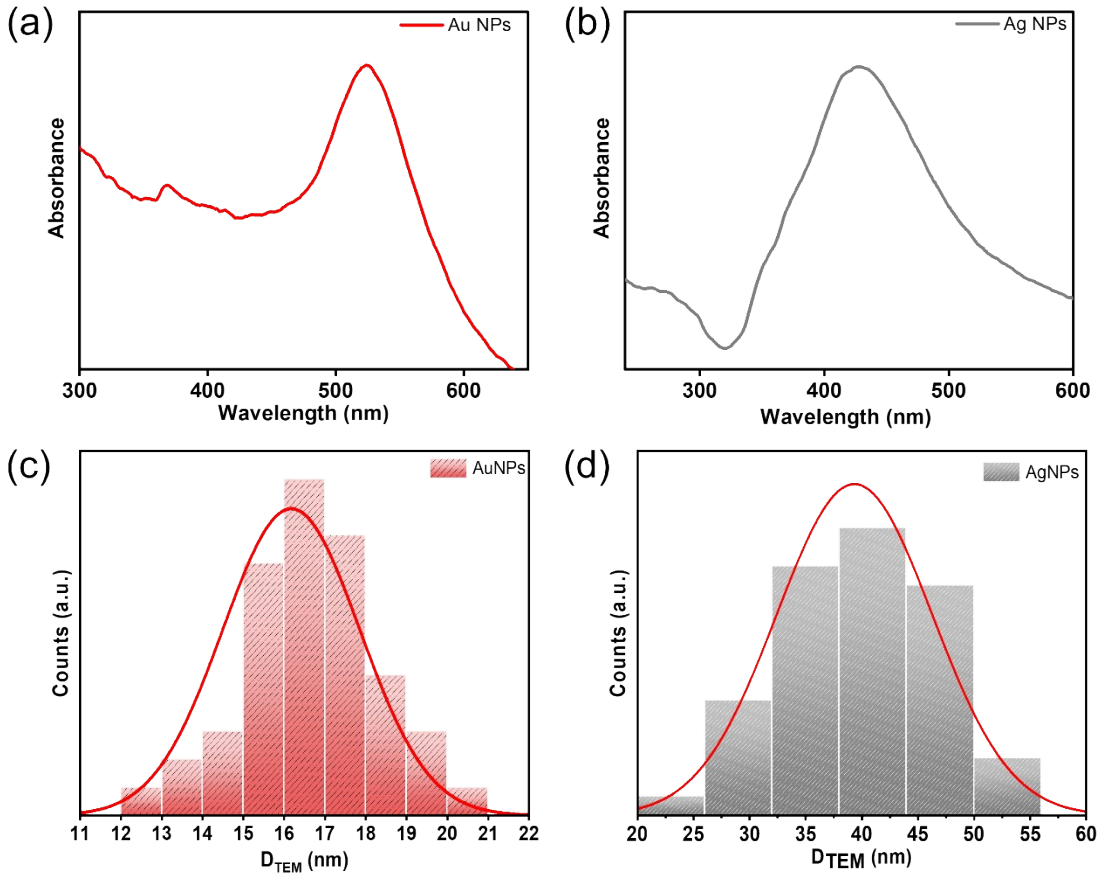

Figure S22. UV-Vis absorption spectra of the synthesized plasmonic nanoparticles. (a) Au nanoparticles exhibiting a characteristic LSPR band centred at ~520 nm and (b) Ag nanoparticles showing an LSPR peak near ~421 nm, confirming their plasmonic behaviour in the visible region. Corresponding particle-size distribution histograms of (c) Au nanoparticles and (d) Ag nanoparticles obtained from TEM analysis reveal average particle sizes of ~16 nm and ~39 nm, respectively. The red curves represent Gaussian fitting of the corresponding nanoparticle size distributions.

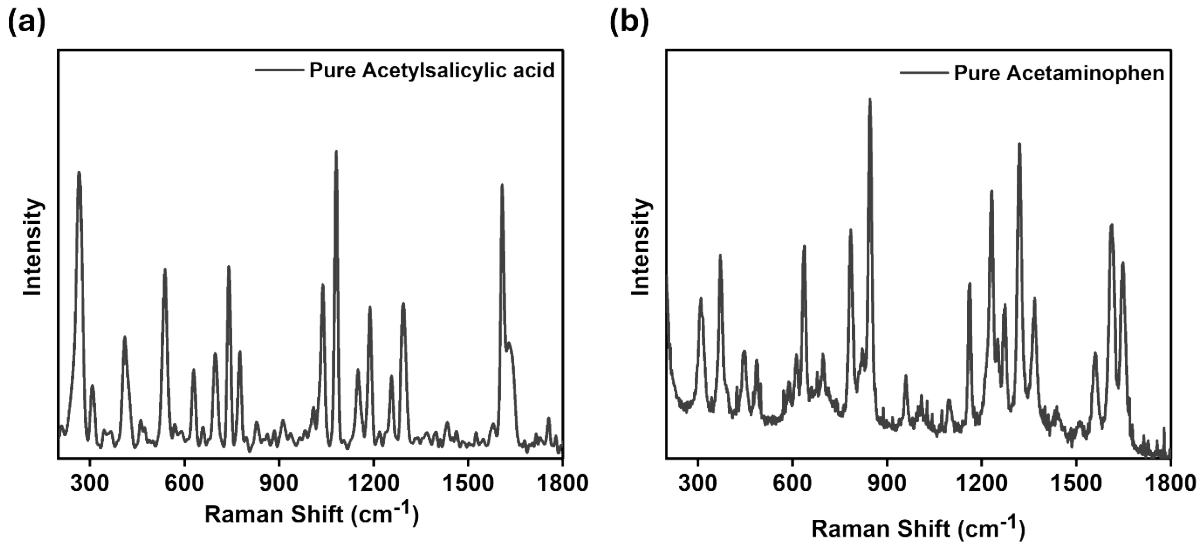

Figure 23. Raman spectra of pure (a) acetylsalicylic acid and (b) acetaminophen

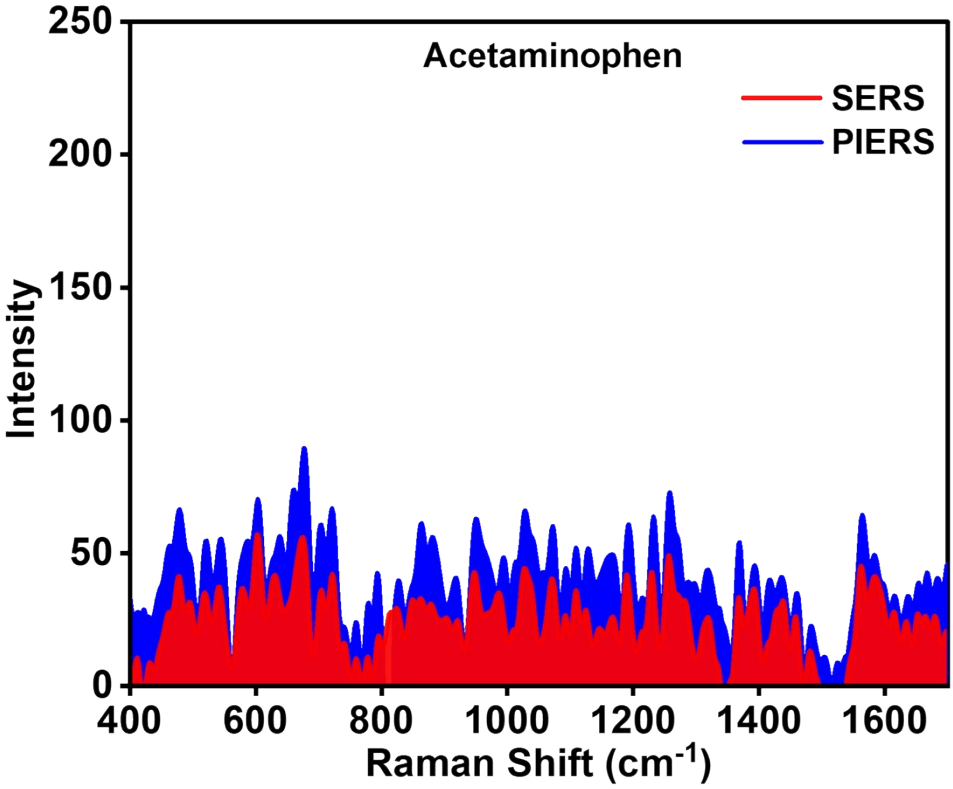

Figure S24. Raman spectra of acetaminophen recorded under SERS (red) and PIERS (blue) conditions using Ti_3C_2/UiO-66-NH_2@Ag hybrid substrate. The PIERS condition involved 40 minutes of UV pre-irradiation followed by spectral acquisition under continuous UV exposure at 785 nm excitation. As mentioned, there is no significant enhancement in the Raman intensity when silver nanoparticles are used.

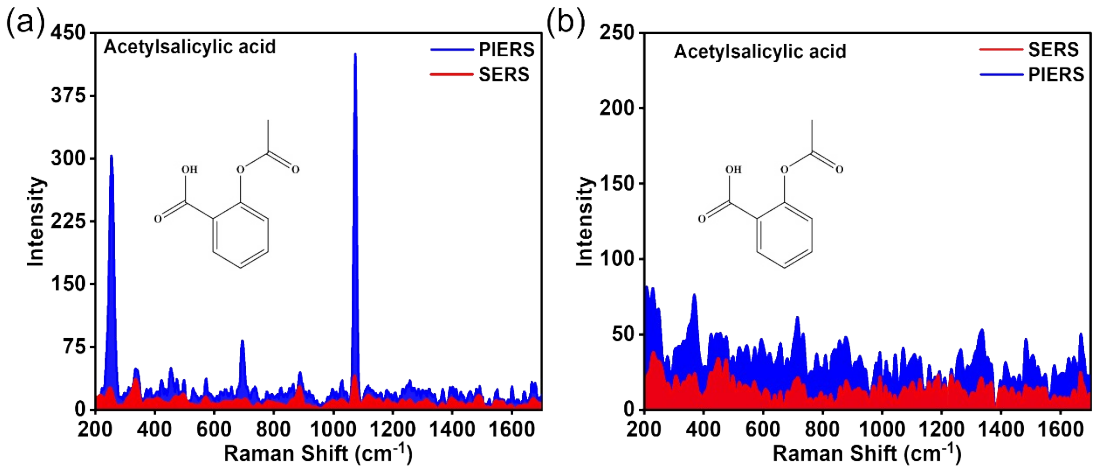

Figure S25. (a) Raman spectra of acetylsalicylic acid under SERS and PIERS conditions using Ti_3C_2/UiO-66-SH_2@Au as the substrate. (b) Corresponding spectra using Ti_3C_2/UiO-66-NH_2@Ag hybrid. In case of (a), PIERS (blue) leads to enhanced peak intensities compared to SERS (red). The molecular structures are shown for reference. UV pre-illumination was carried out for 40 minutes.

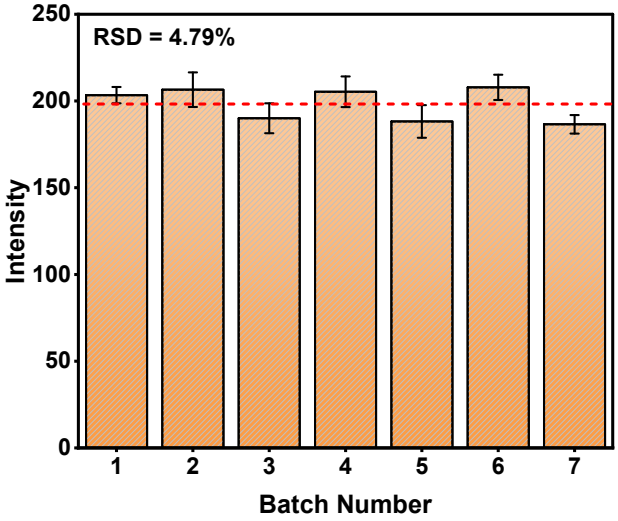

Figure S26. Batch-to-batch variation of the Raman intensity at 1321 cm^{-1} for acetaminophen, demonstrating good fabrication reproducibility. The bar height represents the mean Raman intensity of each batch, obtained from measurements at five different spots per batch. Error bars indicate the standard deviation of intensities measured across the five spots within each batch. The overall batch-to-batch relative standard deviation (RSD) across the seven

independently prepared batches was 4.79%, indicating good substrate reproducibility. The dashed red line represents the average intensity across all batches.

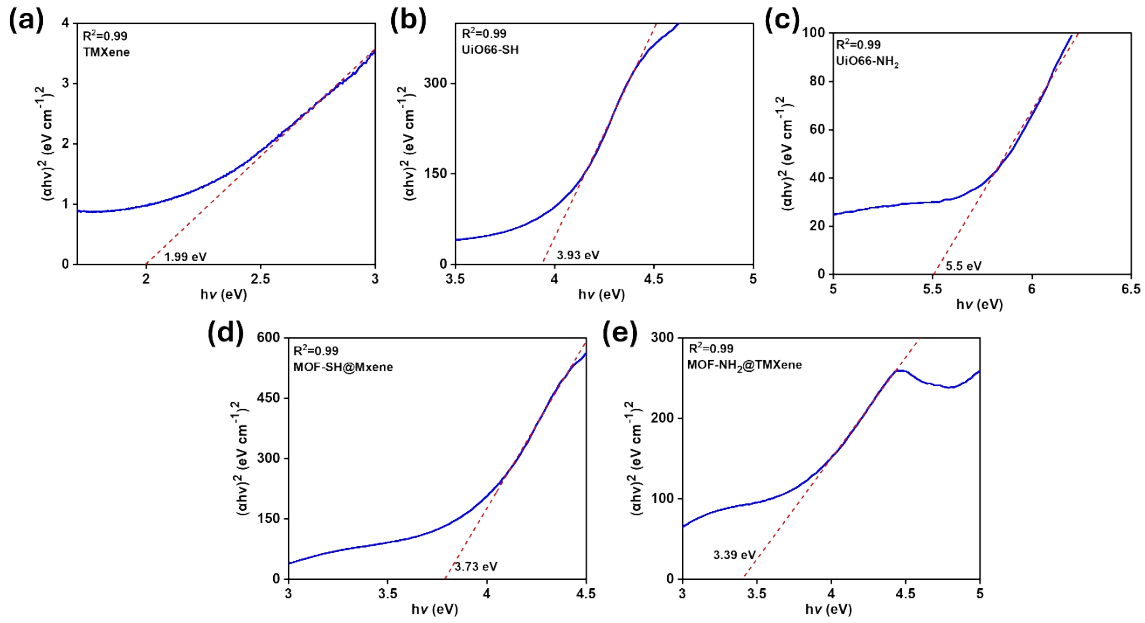

Figure S27. Tauc plots used to estimate the optical band gaps of (a) Ti_3C_2, (b) UiO-66-SH_2, (c) UiO-66-NH_2, (d) Ti_3C_2/UiO-66-SH_2@Au, (e) Ti_3C_2/UiO-66-NH_2@Ag. Band gaps were extracted by linear fitting of the absorption edge and extrapolating the intercept on the energy axis. The narrowing of the bandgap in the hybrid structures confirms successful electronic coupling between UiO-66 and Ti_3C_2.

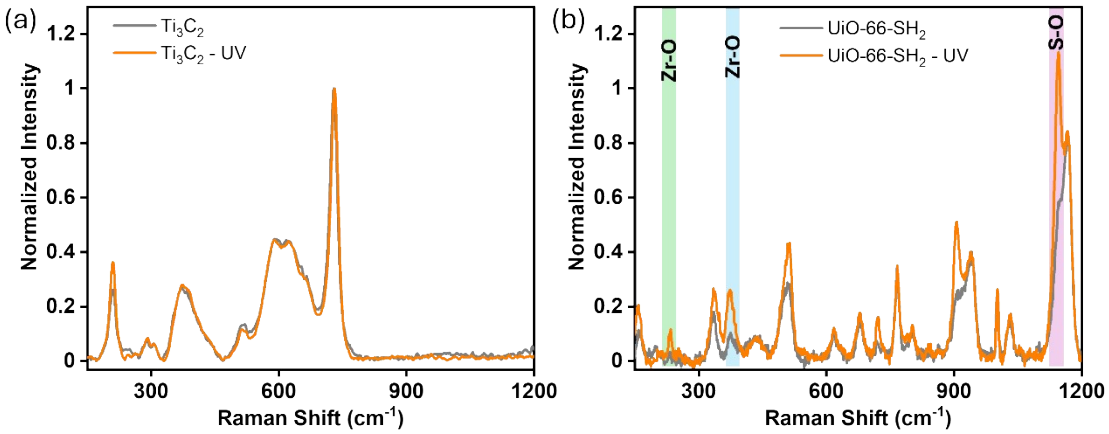

Figure S28. Raman spectra of (a) Ti_3C_2 MXene and (b) UiO-66-SH_2 before and after UV irradiation, which show the change in Zr-O coordination environment after UV illumination. The oxidation of SH is also mentioned in the Raman spectrum after illumination using ultraviolet radiation.

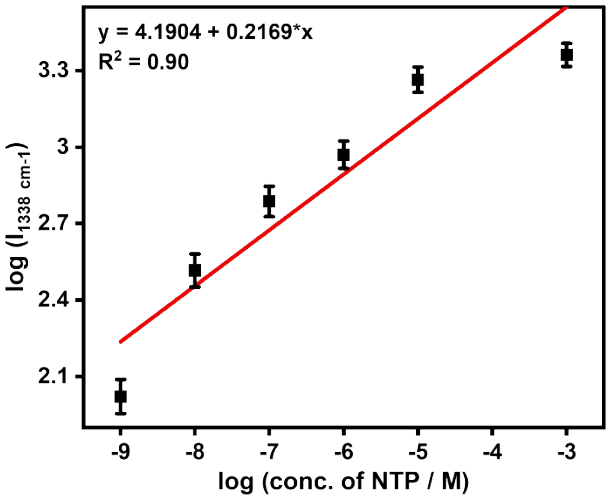

Figure S29. Calibration curve obtained from concentration-dependent PIERS measurements of 4-nitrothiophenol (4-NTP) on the $Ti_3C_2T_x$/UiO-66-SH_2@Au hybrid substrate. The linear fit (red line) was used to determine the analytical response and estimate the limit of detection (LOD). Each data point represents the mean Raman intensity obtained from four independent measurements, while the error bars indicate the standard deviation of the corresponding measurements.

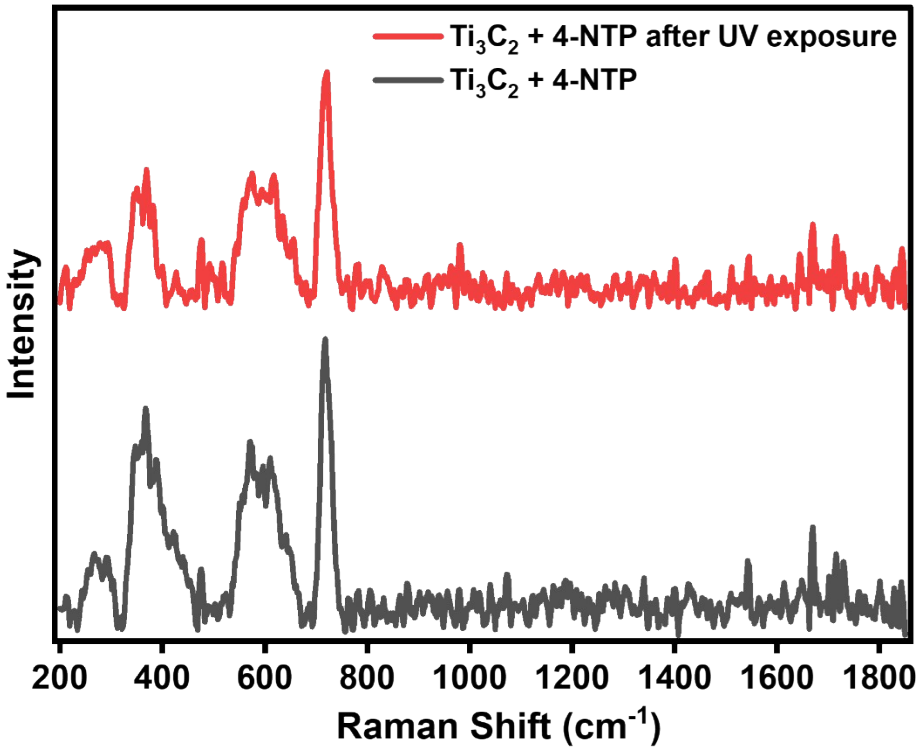

Figure S30. Raman spectra of 4-nitrothiophenol (4-NTP) recorded on Ti_3C_2 MXene under SERS and PIERS conditions. The negligible Raman response indicates that MXene alone does not provide significant Raman enhancement under the experimental conditions.

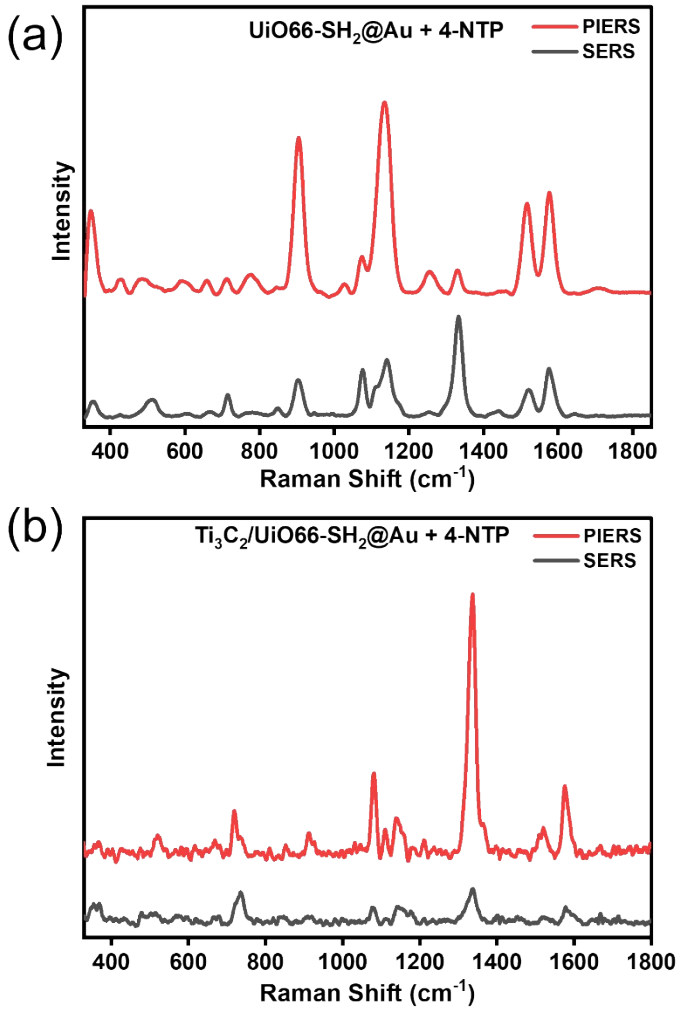

Figure S31. (a) Raman spectra of 4-NTP recorded on UiO-66-SH_2@Au under SERS and PIERS conditions. No significant increase in the Raman intensity of the probe molecule is observed under UV illumination, while MOF vibrational features become more pronounced, (b) Raman spectra of 4-NTP on hybrid 1 under SERS and PIERS conditions, which show the enhanced Raman intensity, showing the efficient transfer of electrons from the hybrid to the analyte molecule.

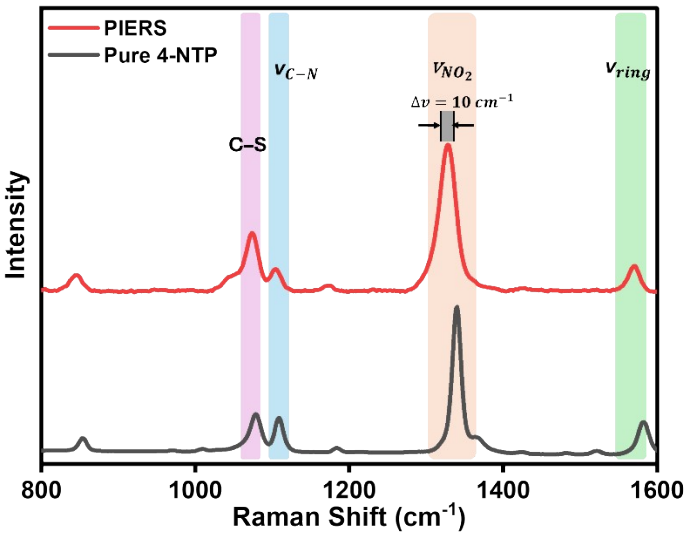

Figure S32. Raman spectrum of pure 4-NTP and the corresponding PIERS spectrum recorded on the Ti_3C_2/UiO-66-SH_2@Au hybrid substrate. The ν(NO_2) vibrational band near 1337 cm^{-1} exhibits a red shift in the PIERS spectrum, indicating modification of the electronic environment of the molecule due to substrate–molecule charge transfer.

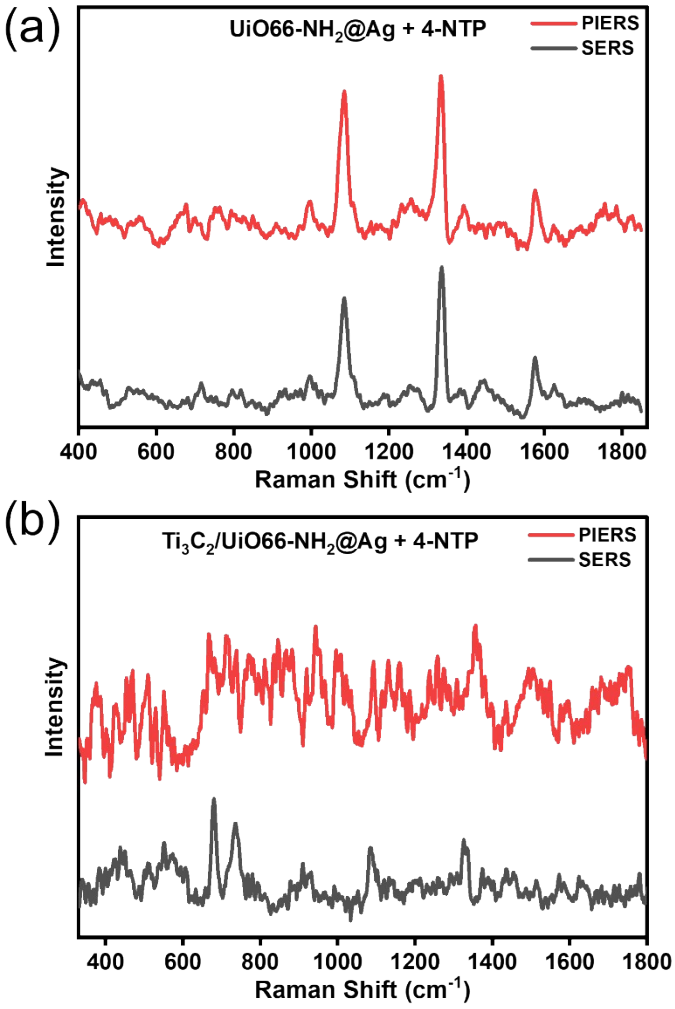

Figure S33. (a) Raman spectra of 4-nitrothiophenol (4-NTP) recorded on UiO-66-NH_2@Ag under SERS and PIERS conditions, showing negligible enhancement under UV illumination, (b) Raman spectra of 4-NTP on the hybrid 2 under SERS and PIERS conditions, where no significant PIERS enhancement is observed, consistent with inefficient photo-induced charge transfer to the analyte molecule.

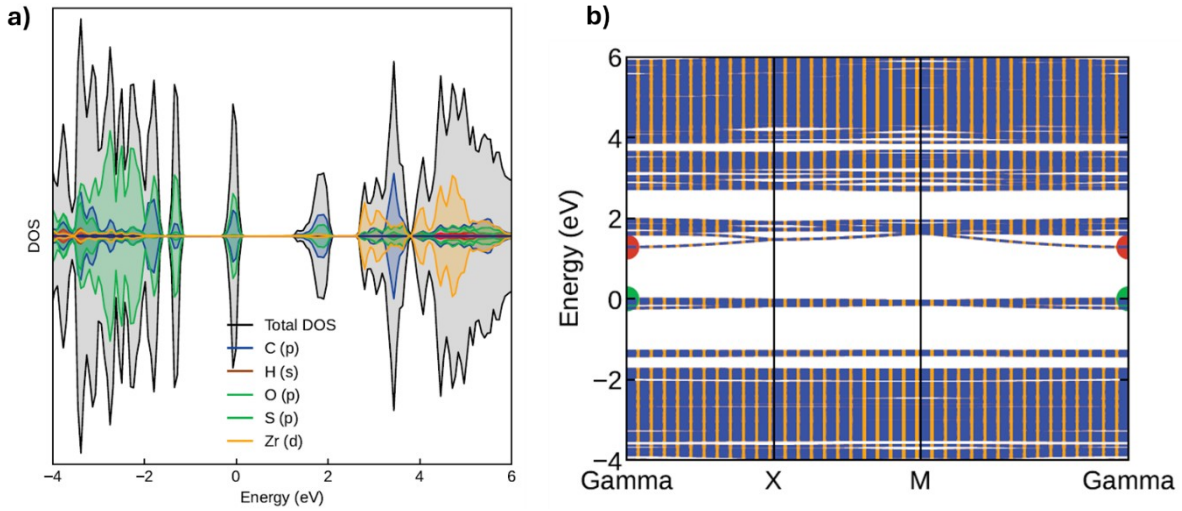

Figure S34. (a) Total and projected density of states, (b) band structure of UiO-66-SH_2.

References

1. S. Mohapatra, S. Siddhanta, D. R. Kumar, C. Narayana and T. K. Maji, *European Journal of Inorganic Chemistry*, **2010**, 2010, 4969-4974.
2. M. Chen, R. Solarska and M. Li, *The Journal of Physical Chemistry C*, **2023**, 127, 2728-2734.
3. Q.-D. Mai, D. Thi Hanh Trang, T. Ngoc Bach, V. Thi Le Na, A.-T. Pham and A.-T. Le, *RSC Advances*, **2025**, 15, 4149-4162.
4. S. Ben-Jaber, W. J. Peveler, R. Quesada-Cabrera, E. Cortés, C. Sotelo-Vazquez, N. Abdul-Karim, S. A. Maier and I. P. Parkin, *Nature Communications*, **2016**, 7, 12189.
5. J.-H. Fu, Z. Zhong, D. Xie, Y.-J. Guo, D.-X. Kong, Z.-X. Zhao, Z.-X. Zhao and M. Li, *Angewandte Chemie International Edition*, **2020**, 59, 20489-20498.
6. Y. Zhang, C. Xue, Y. Xu, S. Cui, A. A. Ganeev, Y. V. Kistenev, A. Gubal, V. Chuchina, H. Jin and D. Cui, *Nano Research*, **2023**, 16, 2968-2979.
7. A. K. Dhillon, A. Thakur, G. S. Kumar, M. B. Choudhary, V. R. Hathwar, S. Barman, R. S. Payal, R. Lo, S. Siddhanta and K. Jayaramulu, *Advanced Optical Materials*, **2025**, 13, e00856.
8. Aastha, R. Lo, S. Ippili, S. Sharma, A. Ajith, M. Trau, S. Kment, C. Narayana, S. Siddhanta and K. Jayaramulu, *Chemistry – An Asian Journal*, **2025**, 20, e00789.
9. M. Pramanik, M. V. Limaye, P. K. Sharma, M. Mishra, S. K. Tripathy and S. B. Singh, *ACS Applied Materials & Interfaces*, **2024**, 16, 29121-29131.
10. R. Singh, A. Thakur, R. Lo, K. Jayaramulu and S. Siddhanta, *Small*, **2025**, 21, 2503180.